# Dynamics of quiescent prominence fine structures analyzed by 2D non-LTE modelling of the H $\alpha$ line

S. Gunár, P. Mein, B. Schmieder, P. Heinzel, N. Mein

A&A 543, A93 (2012)
DOI: 10.1051/0004-6361/201218940


Astronomy & Astrophysics

# Dynamics of quiescent prominence fine structures analyzed by 2D non-LTE modelling of the H$\alpha$ line$^\star$

S. Gunár[1,2], P. Mein[2], B. Schmieder[2], P. Heinzel[1], and N. Mein[2]

[1] Astronomical Institute, Academy of Sciences of the Czech Republic, 25165 Ondřejov, Czech Republic
e-mail: gunar@asu.cas.cz
[2] LESIA, Observatoire de Paris, CNRS, UPMC Paris06, Université Paris Diderot, 5 place Jules Janssen, 92195 Meudon, France

Received 1 February 2012 / Accepted 5 April 2012

**ABSTRACT**

*Aims.* We analyze the dynamics of the prominence fine structures of a quiescent prominence observed on April 26, 2007 during a coordinated campaign of several spaceborne and ground-based instruments. We use Lyman spectra observed by SOHO/SUMER and the H$\alpha$ line spectra obtained by MSDP spectrograph working at the Meudon Solar Tower.
*Methods.* We employ the 2D multi-thread prominence fine-structure modelling that includes randomly distributed line-of-sight (LOS) velocities of individual threads to derive models producing synthetic Lyman lines in good agreement with the SOHO/SUMER observations. We then use these models to produce synthetic H$\alpha$ line spectra that we compare with the observed spectra using three statistical parameters: the line integrated intensity, the line full-width at half-maximum (FWHM), and the Doppler velocity derived from shifts of the line profiles.
*Results.* We demonstrate that the 2D multi-thread models that produce synthetic Lyman spectra in agreement with observations also generate synthetic H$\alpha$ spectra in good agreement with the observed ones. The statistical analysis of the FWHM and Doppler velocities of the synthetic H$\alpha$ line profiles show that the overall LOS velocities in the April 26, 2007 prominence at the time of the observations were below 15 km s$^{-1}$ and in the prominence core were close to 10 km s$^{-1}$. In combination with the analysis of the Lyman spectra, we determine several physical parameters of the observed prominence fine-structures that show that the April 26, 2007 prominence had a relatively low-mass weakly magnetized structure. We are also able to impose some constraints on the prominence core temperature, which may be relatively low, with values below 6000 K.
*Conclusions.* The combination of 2D non-LTE prominence fine-structure modelling with the statistical analysis of the observed and synthetic Lyman and H$\alpha$ spectra allows us to analyze the influence of the model input parameters and the velocity fields on the synthetic H$\alpha$ line profiles, thus determine the overall dynamics of the observed prominence as well as the physical parameters of its plasma.

**Key words.** Sun: filaments, prominences – radiative transfer – line: profiles – techniques: spectroscopic – methods: data analysis – methods: statistical

## 1. Introduction

A coordinated observational campaign of spaceborne instruments onboard SOHO (SOlar and Heliospheric Observatory), Hinode, and TRACE (Transition Region and Coronal Explorer) and several ground-based instruments including the Meudon/MSDP (Multichannel Subtractive Double Pass) spectrograph working at the Meudon Solar Tower (Mein 1991) have yielded an extensive set of observations of a quiescent prominence passing over the limb in three consecutive days from April 24 to April 26, 2007. This set contains high-resolution UV spectra and also high-resolution imaging and spectral information about the whole prominence in the H$\alpha$ line. Since such extensive quasi-simultaneous multi-channel observations of prominence are rare, this prominence has been studied by several authors.

Among them, Heinzel et al. (2008) studied the prominence occurring on April 25, 2007 in multiple spectral channels ranging from X-rays to the optical-range H$\alpha$ line and showed the importance of the emissivity blocking phenomena when analyzing of quiescent prominences and their accompanying cavities. Schmieder et al. (2010) and Berger et al. (2010) analyzed the dynamics of the prominence fine structures observed on the same day. Török et al. (2009) studied the prominence observed on April 24, together with the overlaying arcade and the cavity using the X-ray observations. The prominence observed on April 26 (see Fig. 1) was studied by Labrosse et al. (2011) using the He II line and by Berlicki et al. (2011) using multiple instruments and spectral channels. Our present work extends the study of Berlicki et al. (2011) with emphasis on the statistical analyses of the synthetic and observed H$\alpha$ line profiles with focus on the investigation of the prominence fine-structure dynamics.

To obtain the synthetic H$\alpha$ spectra, we use the 2D prominence fine-structure models developed by Heinzel & Anzer (2001), which represent individual prominence fine-structure 2D threads in magneto-hydrostatic (MHS) equilibrium and employ 2D multi-level non-LTE (i.e. departures from local thermodynamic equilibrium) radiative-transfer computations to derive the emerging synthetic hydrogen spectra. These models, in a multi-thread configuration with randomly distributed LOS velocities of individual threads, are able to produce synthetic Lyman spectra (Gunár et al. 2007, 2008, 2010) and also synthetic H$\alpha$ spectra (Berlicki et al. 2011) that are in good agreement with the observations. Moreover, Gunár et al. (2011a) and Gunár et al. (2011b) demonstrated that the temperature and electron density structures of these models lead to the synthetic differential

$^\star$ Appendix A is available in electronic form at http://www.aanda.org

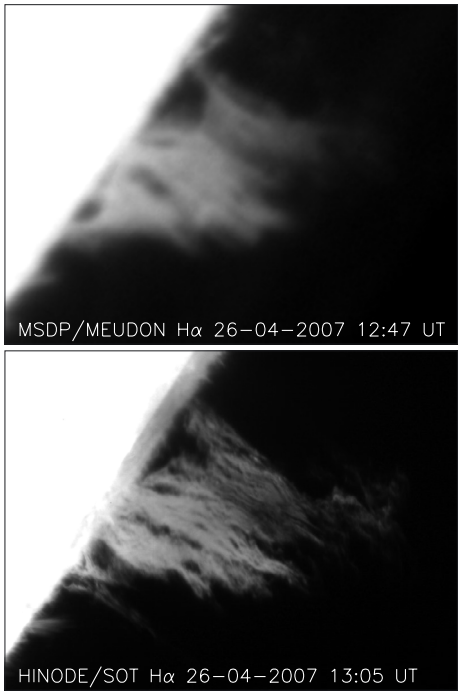


**Fig. 1.** Prominence of April 26, 2007 observed in the H$\alpha$ line. *Top*: observations with the Meudon/MSDP spectrograph. *Bottom*: Hinode/SOT (Solar Optical Telescope, Tsuneta et al. 2008) observations. The field-of-view for all images is about 130″ × 100″. Adapted from Berlicki et al. (2011).

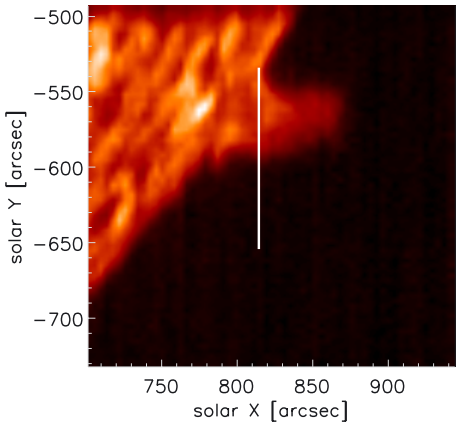


**Fig. 2.** Raster observations of SOHO/CDS (Coronal Diagnostic Spectrometer, Harrison et al. 1995) in the He I 584.33 Å line made on April 26, 2007 between 13:03:34 and 13:30:08 UT. The position of the SOHO/SUMER slit is marked. Courtesy of Schwartz.

emission-measure curves that are also in good agreement with the observations. More on the modelling of prominences can be found e.g. in the review of prominence physics by Labrosse et al. (2010).

The paper is organized in the following way. Section 2 provides a description of the observed Lyman spectra used in this work. Section 3 describes the analyzed H$\alpha$ observations and provides a comprehensive description of their calibration. In Sect. 4, we give a brief description of our 2D prominence fine-structure models. Section 5 presents analyses of the synthetic data obtained by the modelling, including the pixel-to-pixel and statistical analyses of the Doppler velocities. Section 6 provides our discussion and conclusions.

## 2. SOHO/SUMER observations

We use the SOHO/SUMER (Solar Ultraviolet Measurements of Emitted Radiation UV-spectrograph, Wilhelm et al. 1995) observations of the hydrogen Lyman lines (excluding the Lyman-$\alpha$ line that was not observed) to constrain the 2D multi-thread prominence fine-structure models. These were taken in the observational block between 13:01:34 and 23:50:04 UT on April 26, 2007 with the SUMER slit crossing the prominence as indicated in Fig. 2. Here we use only the Lyman-$\beta$ spectra obtained at 13:01:34 UT, and Lyman-$\gamma$ and Lyman-$\delta$ obtained at 13:03:41 UT. These observations were obtained by the detector B with the exposure time of 115 s and with the SUMER slit in the sit-and-stare mode.

The observed spectra were reduced and calibrated using standard SolarSoft procedures developed for SOHO/SUMER data reduction. The following procedures were applied in this order: decompression of binary data saved in IDL-save files, dead-time correction, flat-fielding, local-gain correction, and correction for the geometrical distortion of the detector. Finally, the data were calibrated to intensity units with the *radiometry* procedure (Schühle 2003, priv. comm.)[1]. For line identifications, we used the SOHO/SUMER spectral catalogue (Curdt et al. 2001). The spectral image on the detector is inclined with respect to the detector horizontal line because of the different orientation of the grating and the detector. This causes the spectra of the spectral lines with different wavelengths to be vertically shifted to either higher or lower pixels on the detector. Moreover, there is an additional vertical shift caused by the displacement of the slit image on the detector, which is in turn produced by the nonlinearity of the grating focus mechanism (Schühle 2003). Vertical shifts caused by both effects together were computed for all used lines with the SolarSoft procedure *delta_pixel* and spectra were corrected for mutual shifts.

## 3. Meudon/MSDP H$\alpha$ observations

The prominence observed on April 26, 2007 was part of an extensive very quiescent filament that crossed the limb over three consecutive days between April 24 and April 26. This filament was aligned along a magnetic inversion line surrounded by weak magnetic polarities of a maximum of 10 Gauss in SOHO/MDI magnetograms. The observation was obtained during a solar minimum-activity period. On-the-disk observations performed prior to the filament limb crossing show a weak structure where only the filament feet were clearly detectable, implying that this was a relatively low-mass filament.

In this paper we analyze the H$\alpha$ Meudon/MSDP spectra obtained at 12:47:09 UT (see Fig. 1). In the following section we provide a detailed description of the way in which these H$\alpha$ spectral and imaging observations were obtained, processed, and calibrated.

In general, the Meudon/MSDP observations consist of series of five spectro-images 465″ × 70″ with 16″ overlaps between each pair of time sequences. They were processed with the MSDP software. Figure 3 shows maps of the H$\alpha$ central intensity in three different fields of view: the panel (a) shows the part of the inner solar disk used to determine the H$\alpha$ line-centre wavelength from an average Doppler-shift over a large area; panel (b) shows a field of view including the solar limb together with a

[1] For a detailed technical information about the instrument, corrections, and procedures, see http://www.mps.mpg.de/projects/soho/sumer/text/webluca/ch_iust.html and references therein.

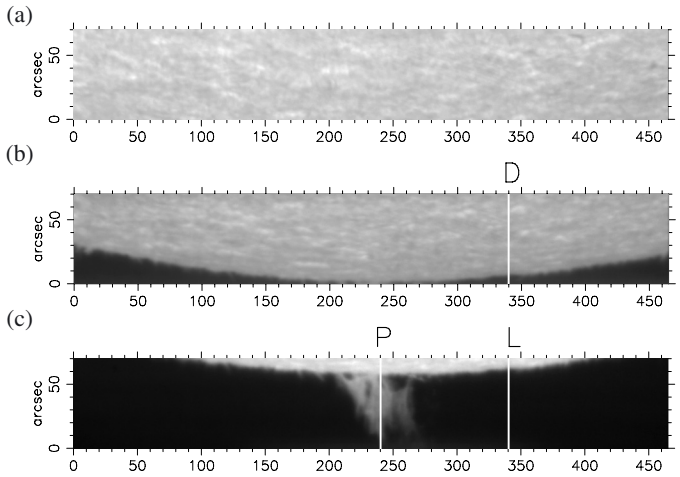


**Fig. 3.** Maps of the Hα central intensity in three fields of view showing: **a)** the inner solar disk area; **b)** part of the solar disk together with the solar limb; **c)** the solar limb and the observed prominence. Cross-sections $D$ ($x$ = 340 arcsec), $L$ ($x$ = 340 arcsec), and $P$ ($x$ = 240 arcsec) are indicated by vertical white lines.

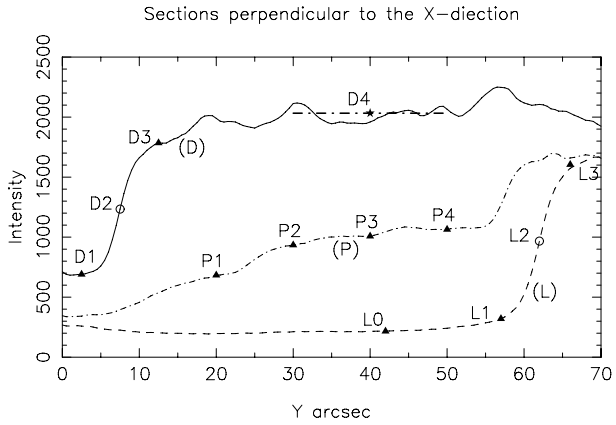


**Fig. 4.** The Hα line-centre intensity (in MSDP signal intensity units) plotted along cross-sections $D$ (solid line), $L$ (dashed line), and $P$ (dot-dashed line) indicated in Fig. 3. Circles indicate points $D2$ and $L2$ representing the position of the chromospheric limb. Points $D1$, $D3$ and $L1$, $L3$ represent the $y$-direction distance of ±5 arcsec from $D2$ and $L2$, respectively.

large disk area necessary for calibration of the absolute Hα central intensity for $\theta$ values not too close to the limb ($\theta < 90°$); and panel (c) shows a map of the prominence itself including the solar limb.

### 3.1. Calibration using the disk Hα profiles

*The relative calibration of maps (b) and (c)*

The $x$ and $y$ coordinates of the maps given in Fig. 3 roughly represent the directions parallel and perpendicular to the solar limb. We extract cross-sections $D$ and $L$ from maps (b) and (c) at the same $x$-coordinate and outside the prominence, respectively, to record the sky background up to the limb. In Fig. 4, we plot the intensity measurements at the Hα centre along the $D$ (solid line) and $L$ (dashed line) cross-sections. Owing to the 16 arcsec $y$-direction overlap between maps (b) and (c), the position of the limb is visible in both curves. The wavelength of the Hα line centre was determined in such a way that the mean Doppler shift of all line profiles contained in the map (a) is equal to zero. The line intensities are smoothed across ±5 arcsec along the map's $x$-direction to reduce the effects of noise and the solar fine structures. Points $D2$ and $L2$ indicated by circles in the Fig. 4 are the inflection points defining the position of the chromospheric limb and correspond to the same location on the Sun. Points $D1$, $D3$ and $L1$, $L3$ represent the $y$-direction distance of ±5 arcsec from $D2$ and $L2$, respectively.

The background intensities at cross-sections $D$ and $L$ are different (see Fig. 4). At each cross-section, the background intensity consists of two components. The first one is the so-called sky solar spectrum – the light scattered in the Earth's atmosphere. The second one is mainly the light scattered by the spectrograph, which is roughly proportional to the area of the solar disk going through the field stop that is larger for $D$ than for $L$.

If there is any difference between the exposure times of maps (b) and (c), it can be deduced from the ratio

$$r = (I_{L3} - I_{L1}) \,/\, (I_{D3} - I_{D1}) = 1.173, \quad (1)$$

where $I_{L3}, I_{L1}, I_{D3}$, and $I_{D1}$ are the intensities in $L1$, $L3$ and $D1$, $D3$.

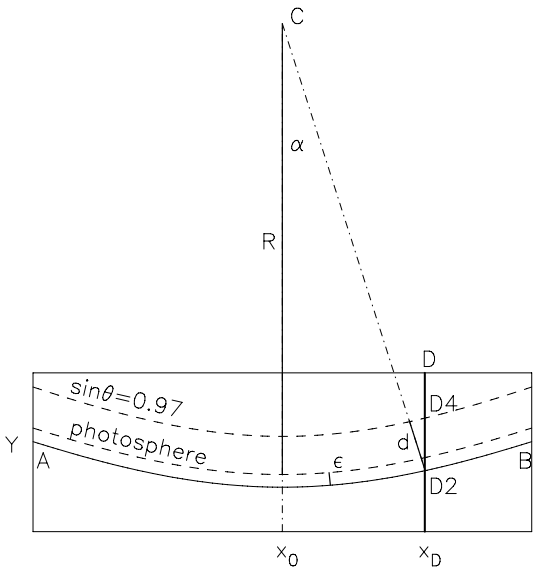


**Fig. 5.** The rectangle corresponds to the field of view of the map (b) of Fig. 3. Point $C$ represents the centre of the solar disk. The solid curve between points $A$ and $B$ represents the chromospheric limb. $D4$ is the point used for the absolute calibration.

*Search for a reference Hα profile*

We can calibrate the data using David reference profiles (David 1961) at a $\theta$-value roughly corresponding to a middle point $D4$ of the cross-section $D$, at sin $\theta = 0.97$ (see Fig. 4). The distance of the chromospheric limb from a point corresponding to a given $\theta$-value (see Fig. 5) is

$$d = \epsilon + R(1 - \sin\theta), \quad (2)$$

where $R$ is the photospheric solar radius and $\epsilon$ the apparent distance between the photospheric and chromospheric limbs.

The cross-sections $D$ and $L$ are not exactly perpendicular to the solar limb. Their respective angle is given by

$$\sin\ \alpha = (x_D - x_0)/(R + \epsilon), \quad (3)$$

where $x_0$ is the abscissa of the point where the limb is parallel to the $x$-direction (Fig. 5). This point can be found by determining the axis of symmetry of any cross-section parallel to the

$x$-direction that is crossing the solar disk. We find $x_0$ to be equal to 246 arcsec by determining the middle point between inflection points (locations of the limb) of the H$\alpha$ central intensity curve drawn along the upper edge of the map (c) of Fig. 3.

The $y$-direction distance from the chromospheric-limb location $D2$ to the middle point $D4$ is then given by

$$y_{D4} = y_{D2} + d/\cos\ \alpha. \quad (4)$$

With $\epsilon = 3$ arcsec and $\sin\ \theta = 0.97$, we get $\alpha = 5.6°$, $d = 31.8$ arcsec, and $y_{D4} = 39.4$ arcsec. We use the point $D4$ as the location of the reference H$\alpha$ profile used for absolute calibration.

*Absolute calibration*

In Fig. 4, we plot the point $D4$ corresponding to the H$\alpha$ central-intensity value $I_{D4}$ that is the average value over the area specified by ±10 arcsec in the $y$-direction and ±20 arcsec in the $x$-direction around $D4$. Such a large area is necessary to get a reliable average value for the absolute calibration.

To derive the background intensity, we use the cross-section $L$ and point $L0$ (see Fig. 4) located at a sufficient distance away from both the solar limb and the edge of the field of view.

We derive the absolute intensity calibration for the data contained in the map (c) of Fig. 3. The intensity signal $I_{\rm MSDP}$ measured above the local background with the exposure time of the map (c) is

$$I_{\rm MSDP} = (I_{L3} - I_{L0}) + r\,(I_{D4} - I_{D3}) = 1679. \quad (5)$$

This value must be compared to the intensity of the solar disk at $\sin\ \theta = 0.97$, according to David (1961). By interpolating between $\sin\ \theta = 0.95$ and $\sin\ \theta = 0.98$ we deduce that

$$I_{\rm David} = 5.13 \times 10^{-6}\ {\rm erg\ cm^{-2}\ sr^{-1}\ s^{-1}\ Hz^{-1}}. \quad (6)$$

The calibration coefficient of MSDP signal intensities is

$$C = I_{\rm David}/I_{\rm MSDP} = 3.05 \times 10^{-9}. \quad (7)$$

The uncertainty in this calibration depends on several factors. In Eq. (5), $(I_{D4} - I_{D3})$ is much smaller than $(I_{L3} - I_{L0})$, so small errors in $r$ do not modify the result significantly. In the same way, possible fluctuations of the background intensity between $L0$ and $L3$ (see Fig. 4, dashed line) are probably small, as are departures between calibrations of different MSDP channels. The most important uncertainty seems to be due to solar chromospheric fluctuations around $D4$, despite the averaging we use around this point (see Fig. 4, solid line). Globally, we may expect errors of the order of 10% in the $C$ factor.

### 3.2. Scattered light correction and Gaussian-type prominence Hα profiles

*Method.* To allow an accurate comparison of the observed H$\alpha$ profiles, with the synthetic profiles we process the prominence data corresponding to the map (c) of Fig. 3 by: i) taking into account the background fluctuations across the field of view; ii) using Gaussian interpolated profiles that are more suitable than cubic-spline interpolated ones.

*Background corrections.* We define 25 arcsec-wide intervals in the $x$-direction $s1$, $s2$, $s3$, and $s4$ around four points located outside the prominence area along a cross-section parallel to the $x$-direction (Fig. 6). Along this cross-section, the background is approximated by a third-degree polynomial using averages over selected intervals. Figure 6 shows the measured H$\alpha$ intensity in the central MSDP channel (number 5), together with the third-degree polynomial approximation of the background intensity.

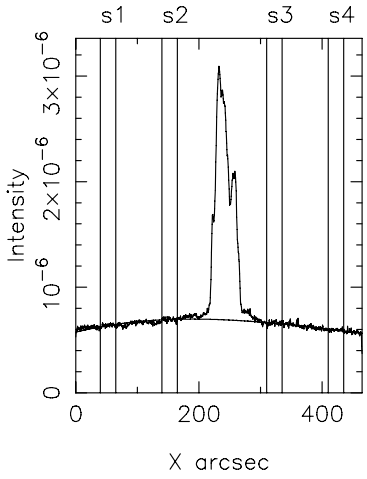


**Fig. 6.** Measured H$\alpha$ intensity in the central MSDP channel plotted along a cross-section parallel to the $x$-direction, together with the third-degree polynomial approximation of the background intensity. Intensity units are in erg s$^{-1}$ cm$^{-2}$ sr$^{-1}$ Hz$^{-1}$.

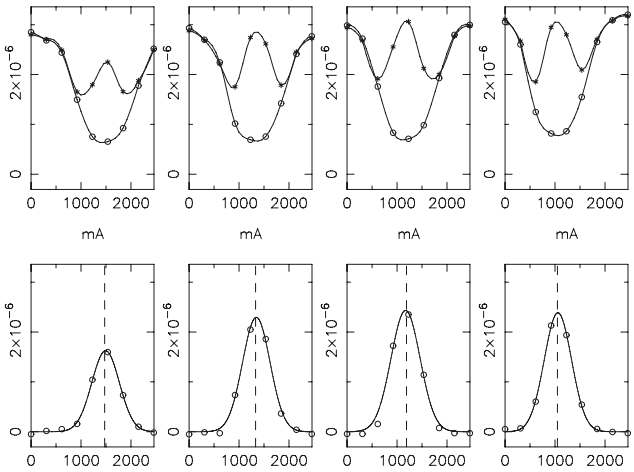


**Fig. 7.** *Top*: background (circles) and prominence profiles (asterisks) with standard cubic-spline interpolation for four points $P1$, $P2$, $P3$, and $P4$ along the cross-section $P$. The wavelength scale shows the wavelength distance to the first MSDP channel. *Bottom*: Gaussian fits of prominence H$\alpha$ profiles corresponding to the same points. Dashed lines show the line-centre position corresponding to zero LOS velocity. Intensity units are in erg s$^{-1}$ cm$^{-2}$ sr$^{-1}$ Hz$^{-1}$.

The prominence H$\alpha$ emission profile is obtained by subtracting the background. Figure 7 (top) shows the background (circles) and the prominence profiles (asterisks) with standard cubic spline interpolation for four points $P1$, $P2$, $P3$, and $P4$ along the cross-section $P$ (see Fig. 4). The wavelength scale shows the wavelength distance to the first MSDP channel.

*Gaussian profiles.* To allow for a simple comparison between observed and synthetic H$\alpha$ line profiles, we fit Gaussian functions to the MSDP data after subtraction of the background. From each profile, we extract the maximum intensity point and four additional values: two intensities from the blue and two from the red part of each profile. Any negative values are substituted by zeros, and the maximum signal intensities lower than 100 counts in MSDP signal intensity units (as in Fig. 4) are

excluded. We denote $I_j$ the five extracted intensities. We compute a second-degree least squares polynomial $P(\lambda)$ from values of $\log(I_j)$ with weights equal to $I_j^2$. Figure 7 (bottom) shows the profiles

$$G(\lambda) = e^{P(\lambda)} \tag{8}$$

obtained at the points $P1$, $P2$, $P3$, and $P4$ along the cross-section $P$.

*Reference of zero LOS velocities.* If Doppler-shifts deduced from Gaussian profiles are referred to the same line-centre wavelength as disk profiles, the resulting average velocity is not exactly zero. This may be due to small asymmetries in the line cores. Any factor acting in a different way on absorption and emission profiles, such as calibration uncertainties or telluric lines, can produce such a discrepancy. However, the prominence under study seems to be very quiet. It is seen as a quiescent filament three and four days before, and as a similar prominence one day before. Hence, we assume that it is reasonable to refer the prominence Doppler velocities to a mean value, averaged over the full prominence and weighted by the integrated intensities of individual profiles. The dashed lines drawn in Fig. 7 (bottom) show the line-centre position corresponding to zero LOS velocity.

## 4. Prominence fine-structure models

To obtain the synthetic Lyman and H$\alpha$ line profiles, we employ 2D models depicting the fine structures of prominences in the form of vertically infinite two-dimensional threads embedded in a horizontal magnetic field. These 2D models were developed by Heinzel & Anzer (2001). These threads are uniform in the vertical direction and the variation in all quantities takes place only in the horizontal plane parallel to the solar surface. The 2D threads are in the MHS equilibrium of Kippenhahn-Schlüter type (Kippenhahn & Schlüter 1957) that was generalized to 2D by Heinzel & Anzer (2001) and their temperature structure is specified empirically to encompass both the central cool part and also the prominence-to-corona transition region (PCTR, see Anzer & Heinzel 1999). The PCTR exhibits two distinct forms. In the direction across the magnetic field lines, the temperature rises from the cool core towards the transition region temperatures very rapidly within a narrow PCTR layer, while in the direction along the field the temperature rises gradually within a geometrically much more extended part of the PCTR. This approach is used because the heat conduction is less effective in the direction across the magnetic field lines than along the field. This temperature structure is characterized by an analytic formula

$$T(m,y) = T_{\rm cen}(y) + [T_{\rm tr} - T_{\rm cen}(y)] \left\{ 1 - 4\frac{m}{M(y)} \left[ 1 - \frac{m}{M(y)} \right] \right\}^{\gamma_1}, \tag{9}$$

where $T_{\rm cen}$ is given by

$$T_{\rm cen}(y) = T_{\rm tr} - (T_{\rm tr} - T_0) \left( 1 - \left| \frac{y}{\delta} \right|^{\gamma_2} \right), \qquad \text{for} \qquad |y| \le \delta. \tag{10}$$

Here, the column-mass scale $m$ is parallel to the $x$-direction with a simple relation through the plasma density, where $M(y)$ represents the column-mass integrated in the $x$-direction, and $2\delta$ is the width of the thread perpendicular to the field lines. The temperature $T_0$ represents the minimum temperature at the centre of the thread, $T_{\rm tr}$ is the boundary transition-region temperature at the thread boundaries, and the exponents $\gamma_1$ and $\gamma_2$ describe the temperature gradients within the PCTR, where $\gamma_2$ represents the steep temperature gradient in the direction across the magnetic field lines and $\gamma_1$ is the more gentle gradient along the field. These four parameters, combined with $B_x(0)$ representing the magnetic field strength in the middle of the thread, $M_0$ giving the maximum column density, and $p_{\rm tr}$, which is the value of the gas pressure at the thread boundaries, form the set of input parameters describing the MHS structure of the 2D models. The geometrical dimensions of the 2D thread are determined in the following way: the length of the thread in the $x$-direction (along the magnetic field lines) is the result of the MHS equilibrium and is unique to each set of the model input parameters, while the width of the thread in the $y$-direction (across the field lines) is chosen arbitrarily. We take the value of the thread width to be 1000 km, which is consistent with our previous prominence modelling and approximately represents the spatial resolution of SOHO/SUMER. However, observations of prominences in absorption against the solar disk (as filaments) in the hydrogen H$\alpha$ line, such as those of Lin et al. (2005), indicate that the widths of the prominence/filament fine structures could be as small as 100 km.

To determine the synthetic hydrogen spectra emerging from 2D fine-structure threads, we solve the 2D multi-level non-LTE radiative transfer problem in these fine structures. The details of the method are given in Heinzel & Anzer (2001) and Heinzel et al. (2005).

In the present study, we use multi-thread configurations of the 2D prominence fine-structure models, which are more realistic than single-thread models and can produce synthetic Lyman and Balmer (H$\alpha$) spectra in better agreement with observations (see Gunár et al. 2007, 2008, 2010; Berlicki et al. 2011). Individual threads of these multi-thread models are randomly shifted with respect to the foremost thread (see Fig. 8) to resemble the non-uniformity of the prominence fine structures. The maximum allowed displacement of any thread with respect to the foremost one is in this study equal to a quarter of the thread length. We use multi-thread models consisting of $N$ identical threads without any mutual radiative interaction between individual threads (all parameters are identical for each thread, resulting in identical temperature and electron density structures for all threads). Each thread has a randomly assigned LOS velocity from a given interval. With respect to the method we use, these velocities represent a movement of the fine structures perpendicularly to the magnetic field. However, in reality one does not observe a prominence with LOS strictly perpendicular to the magnetic field lines (we use it for simplicity reasons). If the LOS was not perpendicular but at a non-zero angle with respect to the magnetic field lines, the LOS velocities presented in the multi-thread models could represent the LOS component of the fine-structure movement along the field lines (e.g. flows) or combination of LOS components of all movements.

The multi-thread models with random LOS velocities on the order of $\pm 10\,{\rm km\,s^{-1}}$ allowed us to obtain asymmetric Lyman line profiles in accordance with the observations (Gunár et al. 2008). In this work, we employ the same method to study the effect of the randomly distributed LOS velocities on the synthetic H$\alpha$ line profiles.

## 5. Synthetic data

The prominence studied in this work was previously investigated by Berlicki et al. (2011) who analysed the UV spectra obtained

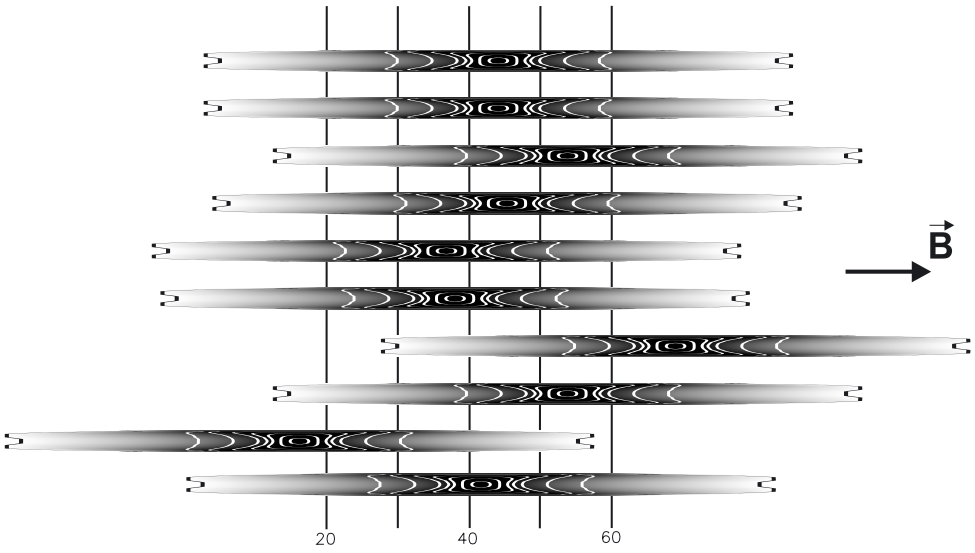


**Fig. 8.** Vertical projection of a randomly generated multi-thread configuration with randomly shifted threads drawn to proper geometrical scale. The orientation of the magnetic field is indicated by an arrow.

by SOHO/SUMER together with H$\alpha$ observations acquired using the Meudon/MSDP spectrograph and HSFA2 (Horizontal-Sonnen-Forschungs-Anlage) spectrograph in Ondřejov (Kotrč 2009). However, these authors used for this investigation the H$\alpha$ spectra only from a very narrow region of the prominence corresponding to the position and the dimensions of the SUMER slit. They also did not analyze in detail the effect of the LOS velocities on synthetic H$\alpha$ profiles. In the present work, we extend their analysis of the H$\alpha$ spectra to the whole prominence and study the effects of several parameters of the multi-thread models on the H$\alpha$ line profiles in greater detail.

We start our investigation with the Model2, which was found by Berlicki et al. (2011) to produce synthetic Lyman spectra in good agreement with observations (see Fig. 9). The synthetic Lyman spectra produced by Model2 exhibit non-reversed line profiles (apart from the Lyman-$\alpha$ profiles that are always reversed), regardless of the orientation of the LOS with respect to the magnetic field (see Berlicki et al. 2011). This appears to be in conflict to the findings of Schmieder et al. (2007), who showed that the Lyman line profiles obtained with the LOS perpendicular to the magnetic field exhibit a central reversal, while those obtained with a LOS parallel to the field show the non-reversed profile shape. However, as discussed by Berlicki et al. (2011) and Gunár et al. (2011b), this dependance of the Lyman line profile shape on the orientation of the LOS is valid only for models of sufficiently high mass. In the case of low-mass, low-pressure models such as Model2 or Model_DEM (Gunár et al. 2011b), even the Lyman lines obtained with LOS perpendicular to the magnetic field exhibit non-reversed profiles.

As shown by Berlicki et al. (2011, see their Fig. 7), one needs to use a multi-thread configuration of the Model2 with approximately 40 threads to obtain synthetic H$\alpha$ profiles and their integrated intensities in agreement with the observations. Because in the present work we analyze the full data set of the H$\alpha$ observations of the April 26, 2007 prominence, we can employ statistical methods to study this prominence in greater detail. Figure 10 shows the scatter plots of the line integrated intensity ($x$-axis) as a function of the line full-width at half-maximum (FWHM, $y$-axis) for the observed data (black diamonds) and the synthetic data of one hundred random realizations of the given model (red crosses). We use only both the observed data with intensities higher than 100 counts in MSDP signal intensity units (as in Fig. 4) and the synthetic data with intensities above the

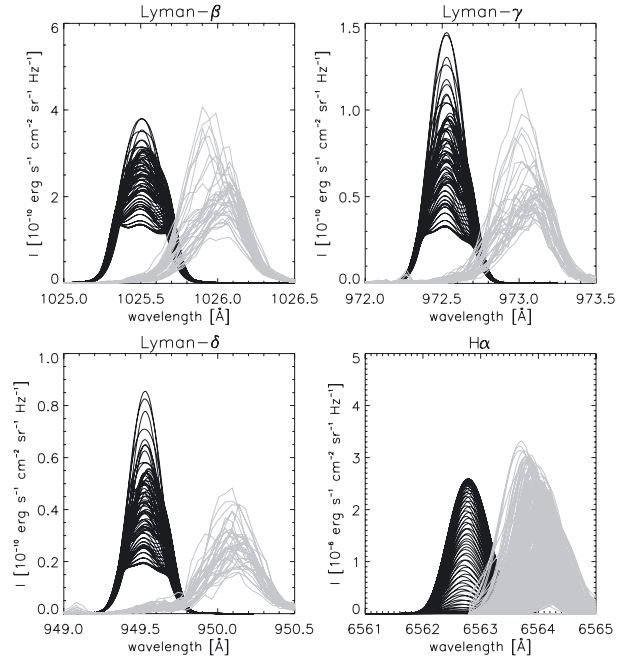


**Fig. 9.** Comparison of observed (gray) and synthetic (black) Lyman lines and H$\alpha$ line. The observed Lyman line profiles from each pixel in the SOHO/SUMER data and observed H$\alpha$ profiles of the whole prominence are plotted. Synthetic data correspond to a randomly generated realization of Model2 with 40 threads and LOS velocities from interval of $\langle -10, 10\rangle$ km s$^{-1}$. Profiles from 83 positions along the foremost thread of the multi-thread model are plotted. The observed profiles are arbitrary shifted in wavelength to allow for an easy comparison.

corresponding intensity cut. Since the integrated intensities are roughly the product of the maximum intensities and the FWHM, the minimum integrated intensities are roughly a linear function of the FWHM, as can be seen in the observed scatter plots. The left panel shows synthetic data of the Model2 with 10 identical threads randomly shifted with respect to the first thread with a maximum displacement of one quarter of the length of the thread, the second panel shows the same model of the multi-thread configuration with 20 threads, and the third panel shows the 40-thread configuration. In all three configurations, the LOS velocities are randomly selected from the interval

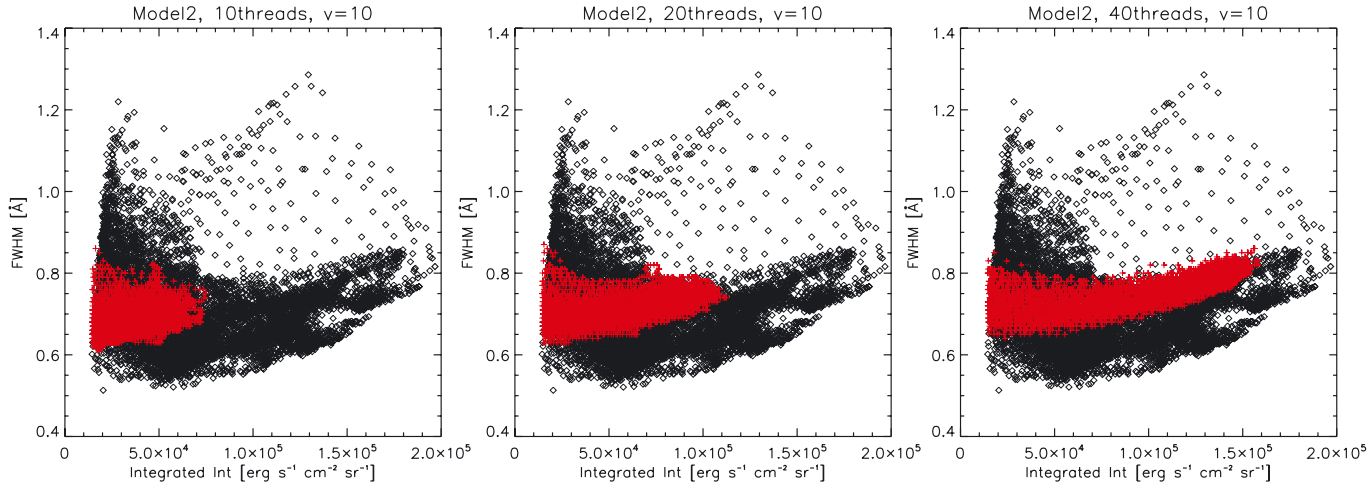


**Fig. 10.** Scatter plots of the integrated intensity ($x$-axis) as a function of the FWHM ($y$-axis). The black diamonds show the observed H$\alpha$ data and the red crosses show the synthetic data from 100 random realizations of the Model2 with 10, 20, and 40 threads and with the LOS velocities from the interval of $\langle -10, 10\rangle$ km s$^{-1}$.

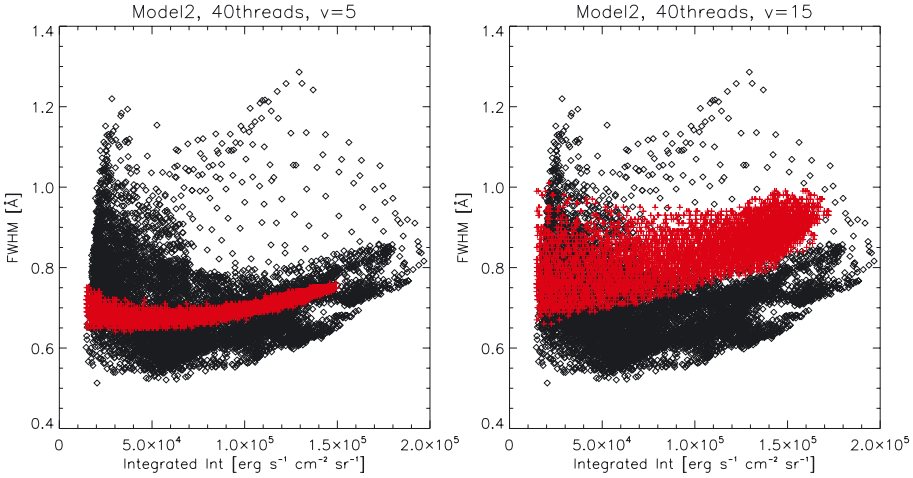


**Fig. 11.** Same as in Fig. 10 but for Model2 with 40 threads and with the LOS velocities from intervals of $\langle -5, 5\rangle$ and $\langle -15, 15\rangle$ km s$^{-1}$.

of $\pm 10$ km s$^{-1}$. It is clear that the 40-thread configurations of the Model2 produce rather reasonable agreement with the bulk of the observed prominence in the integrated intensities but not so much with the line FWHM. The FWHM of the synthetic H$\alpha$ line profiles depends strongly on the choice of the LOS velocity interval, as can be seen from Fig. 11. Here we plot the scatter plots of the line integrated intensity as a function of the line FWHM for the observed data (black diamonds) and the synthetic data (red crosses) of one hundred random realizations of Model2 with 40 threads and LOS velocities from intervals of $\langle -5, 5\rangle$ and $\langle -15, 15\rangle$ km s$^{-1}$. It is clear that the LOS velocities affect mainly the spread of the FWHM towards higher values, while they have a minor effect on the integrated intensities. Figure 11 also shows that the spread in the FWHM of the configuration with LOS velocities from the interval $\pm 15$ km s$^{-1}$, resemble the FWHM spread of the observed data. However, the majority of the observed data have significantly smaller values of the line FWHM and none of the configurations of the Model2 can produce synthetic data in agreement with both the integrated intensities and FWHM at the same time.

To obtain the synthetic H$\alpha$ profiles with FWHM values comparable with those in the observed data, we have to use a modified Model2, where we set the minimum central temperature $T_0$ to 5000 K instead of the value of 8000 K for Model2. We refer to this modified model as Model2_5000 and its parameters are listed in Table 1. The lower central temperature results in a smaller thermal broadening of the synthetic H$\alpha$ profiles, which leads to a reduction in the minimum values of the synthetic data FWHM similar to the observed data. Figures 10 (right panel) and 12 compare Model2 and Model2_5000, which both have 40 threads and LOS velocities from an interval of $\pm 10$ km s$^{-1}$. Although the lower value of the central minimum temperature $T_0$ has a significant effect on the widths of the H$\alpha$ profiles, it does not significantly affect the Lyman line profiles. This, as was argued by Gunár et al. (2011b), is valid only in the case of relatively low-mass, low-pressure models, such as the Model2. In contrast, the variation in $T_0$ has a strong influence on the synthetic Lyman line profiles of more massive models producing reversed profiles when observed across the magnetic field lines. Thus, detailed analyses of the observed H$\alpha$ profiles could allow us to determine the temperature of the cores of the observed prominence fine structures.

All the observed Lyman lines of the April 26, 2007 prominence exhibit non-reversed profiles with relatively low intensities. This data-set does not impose sufficient constraints on the modelling and the trial-and-error method by comparing the observed and synthetic Lyman profiles (a similar prominence was studied by Gunár et al. 2011b). Thus, we are unable to determine a truly unique model for the observed prominence, but we can instead define an area in the parametric space of

**Table 1.** List of input parameters of selected models.

| Model label | Set of input parameters |
|---|---|
| Model2 | $T_0$ = 8000 K; $T_{tr}$ = $10^5$ K; $\gamma_1$ = 5; $\gamma_2$ = 30<br>$B_x(0)$ = 5 Gauss; $M_0$ = $1 \times 10^{-5}$ g cm$^{-2}$;<br>$p_{tr}$ = 0.03 dyn cm$^{-2}$; $p_{cen}$ = 0.035 dyn cm$^{-2}$ |
| Model2_5000 | $T_0$ = 5000 K; $T_{tr}$ = $10^5$ K; $\gamma_1$ = 5; $\gamma_2$ = 30<br>$B_x(0)$ = 5 Gauss; $M_0$ = $1 \times 10^{-5}$ g cm$^{-2}$;<br>$p_{tr}$ = 0.03 dyn cm$^{-2}$; $p_{cen}$ = 0.035 dyn cm$^{-2}$ |
| Model3 | $T_0$ = 8000 K; $T_{tr}$ = $10^5$ K; $\gamma_1$ = 10; $\gamma_2$ = 60<br>$B_x(0)$ = 5 Gauss; $M_0$ = $5 \times 10^{-5}$ g cm$^{-2}$;<br>$p_{tr}$ = 0.015 dyn cm$^{-2}$; $p_{cen}$ = 0.13 dyn cm$^{-2}$ |
| Model3_6000 | $T_0$ = 6000 K; $T_{tr}$ = $10^5$ K; $\gamma_1$ = 10; $\gamma_2$ = 60<br>$B_x(0)$ = 5 Gauss; $M_0$ = $5 \times 10^{-5}$ g cm$^{-2}$;<br>$p_{tr}$ = 0.015 dyn cm$^{-2}$; $p_{cen}$ = 0.13 dyn cm$^{-2}$ |

**Notes.** $T_0$ represents the central minimum temperature; $T_{tr}$ is the boundary transition-region temperature; $\gamma_1$ is the exponent representing the shallower temperature gradient along the field; $\gamma_2$ is the exponent prescribing the steep temperature gradient in the direction across the magnetic field lines; $B_x(0)$ is the magnetic field strength in the middle of the thread; $M_0$ gives the maximum column density in the middle of the thread; $p_{tr}$ represents the boundary gas pressure; and $p_{cen}$ is the central gas pressure derived from the MHS equilibrium.

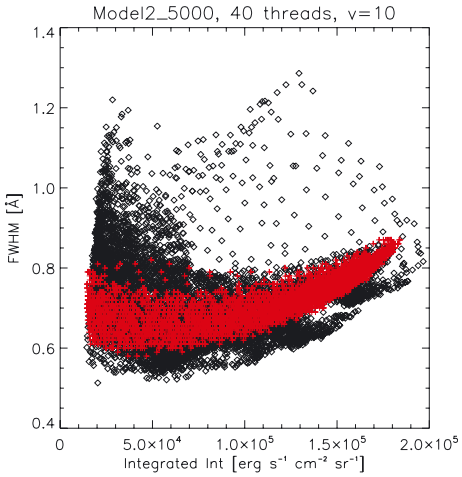


**Fig. 12.** Scatter plots of the integrated intensity ($x$-axis) as a function of the FWHM ($y$-axis). The black diamonds show the observed H$\alpha$ data and the red crosses show the synthetic data from 100 random realizations of the Model2_5000 with 40 threads and with the LOS velocities from the interval of $\langle -10, 10\rangle$ km s$^{-1}$.

the model input parameters, which contains 2D models producing synthetic Lyman spectra in agreement with the observations. However, in contrast to the prominence studied by Gunár et al. (2011b), the April 26, 2007 prominence was also observed in great detail in the H$\alpha$ line. This allows us to determine the number of threads of the multi-thread models needed to produce synthetic H$\alpha$ profiles in agreement with observations (see also Berlicki et al. 2011). We can also investigate the prominence fine-structure core temperature by analyzing the H$\alpha$ line FWHM.

We characterize the parametric space area containing models producing synthetic spectra that agree with observations, by adopting two distinct models, Model2 and Model3, and their variations. Model2 was derived by trial-and-error and used in Berlicki et al. (2011). In this work, the authors did not attempt to determine the uniqueness of this model because the notion

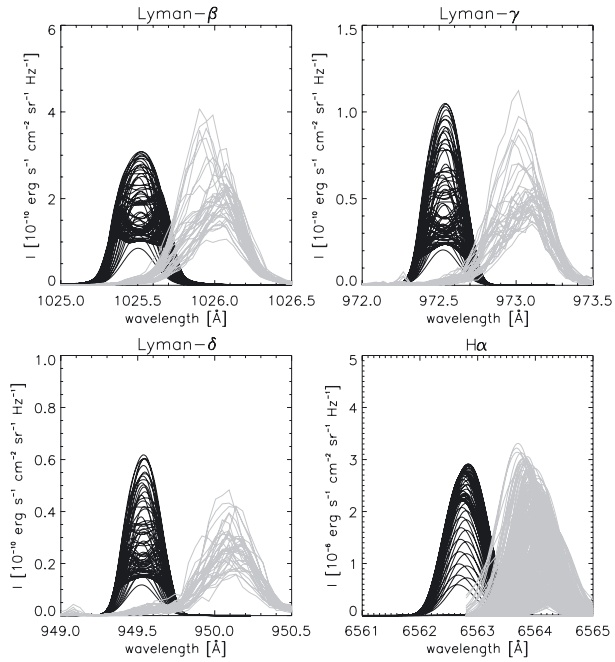


**Fig. 13.** Same as in Fig. 9 but for Model3 with 20 threads and LOS velocities from interval of $\langle -10, 10\rangle$ km s$^{-1}$.

of the parametric space area containing more than one model producing synthetic spectra in agreement with observations was established later by Gunár et al. (2011b). These authors discuss how this parametric space area can be constrained on the one hand by low-mass models producing shallow magnetic dips and nearly isobaric gas-pressure variation and on the other hand by models producing reversed synthetic Lyman lines that thus differ fundamentally from the observed non-reversed Lyman line profiles. Model2 has a relatively low geometrical extension along the magnetic field lines of approximately 6000 km and a rather shallow gas-pressure variation and thus well represents one edge of a suitable parametric space area. The second edge can be represented by Model3, which has steeper gradients of temperature, a higher column mass, and a lower boundary (but higher central) pressure than Model2 (see Table 1). Model3 produces synthetic Lyman lines sometimes already exhibiting slightly reversed profiles (see Fig. 13). The geometrical extension of the Model3 is 20 000 km. Other suitable models are produced by combining input parameters lying in the parametric space between these two models.

Owing to the higher value of the column mass of Model3, a smaller number of threads in the multi-thread configuration is needed to reproduce the observed H$\alpha$ line profiles of the April 26, 2007 prominence. As shown in Fig. 14, 20 threads are sufficient to reproduce the main bulk of the observed data. In this work, we do not attempt to reproduce the synthetic data in complete agreement with the full set of the observed H$\alpha$ data. We assume a relatively uniform model with a multi-thread configuration composed of identical threads, while in the real case of the observed prominence its plasma parameters could vary with the proximity of the prominence edge or the solar surface and of course also within the prominence body. Thus, we can achieve only statistical agreement between synthetic profiles and the most intense part of the observed prominence. The LOS velocities interval of $\pm 10$ km s$^{-1}$ produces rather good agreement between the FWHM of the synthetic H$\alpha$ profiles produced by the Model3 and the observations, apart from the observed profiles

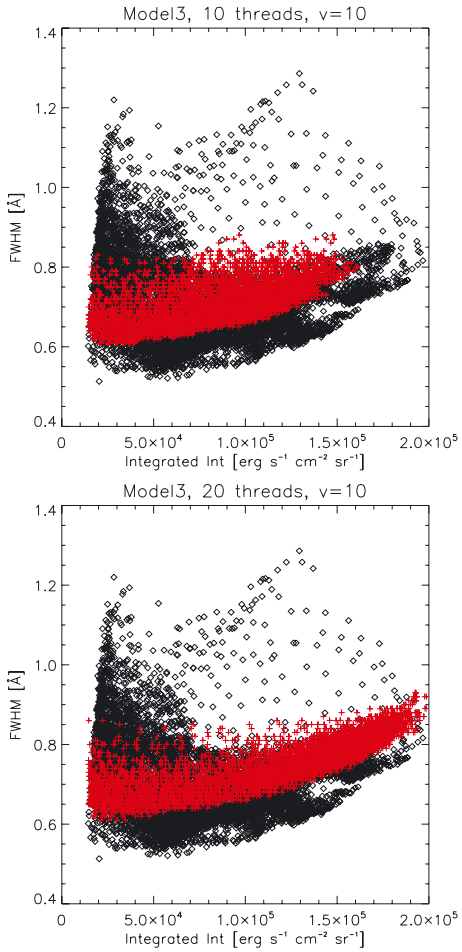


**Fig. 14.** Same as in Fig. 12 but for Model3 with 10 and 20 threads and with the LOS velocities from the interval of ⟨–10, 10⟩ km s$^{-1}$.

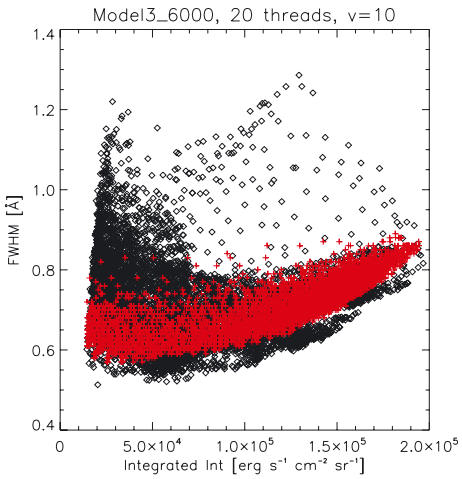


**Fig. 15.** Same as in Fig. 12 but for Model3_6000 with 20 threads and with the LOS velocities from the interval of ⟨–10, 10⟩ km s$^{-1}$.

with the lowest FWHM values. This portion of the observed data can be reproduced only by lowering the central minimum temperature of the model, as in the case of Model2. In this case, we use Model3_6000 with the $T_0$ equal to 6000 K (5000 K leads to a numerically unstable model). Figures 14 (lower panel) and 15 show a comparison between Model3 and Model3_6000 in both 20-thread configurations with LOS velocities from the interval of ±10 km s$^{-1}$.

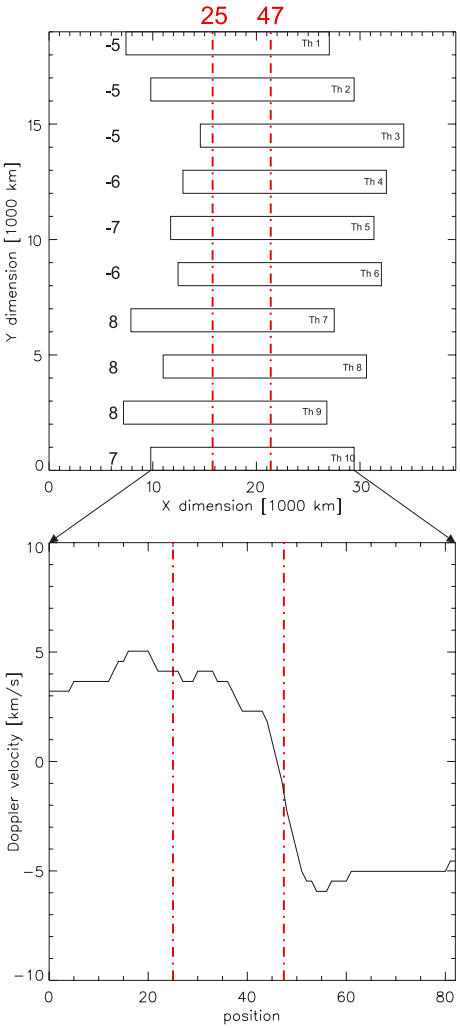


**Fig. 16.** *Top*: special configuration of Model3_6000 consisting of 10 identical threads with fixed geometrical positions and a fixed distribution of the LOS velocities resembling two bundles of fine-structure threads moving in opposite directions. *Bottom*: derived Doppler velocities for 83 positions along the foremost thread of this special multi-thread configuration.

### 5.1. Doppler velocities – pixel-to-pixel analysis

To investigate the behaviour of the Doppler-shift measurements and thus the derived Doppler velocities on a pixel-to-pixel basis in observations and position-to-position basis in synthetic data, we use a special setup of the Model3_6000. This special configuration consists of 10 identical threads with fixed geometrical positions (see Fig. 16, top) and a fixed distribution of LOS velocities resembling two bundles of fine-structure threads moving in opposite directions. We choose this relatively simple distribution of the LOS velocities to allow an easier comprehension of the multi-thread model configuration. However, the conclusions of the pixel-to-pixel analysis are independent of the choice of this special or any other configuration and are valid for any multi-thread configuration where LOS velocities differ from thread to thread, assigned randomly or otherwise.

To trace the formation of the synthetic Hα profiles within the multi-thread model in detail, we use a similar technique to that used by Gunár et al. (2008) to study the asymmetries of the Lyman line profiles. The specific intensity emerging from the multi-thread model at a given wavelength and given position

along the length of the foremost thread in the observers frame is described by the formula (Gunár et al. 2008)

$$I_{\rm total}(\lambda) = [... [[I_{\lambda^{(1)}} \times \exp(-\tau_{\lambda^{(2)}}) + I_{\lambda^{(2)}}] \times \exp(-\tau_{\lambda^{(3)}}) + I_{\lambda^{(3)}}] \times ... + I_{\lambda^{(N-1)}}] \times \exp(-\tau_{\lambda^{(N)}}) + I_{\lambda^{(N)}}, \quad (11)$$

where the intensity produced by the thread $n$ ($I_{\lambda^{(n)}}$) and optical thickness of thread $n$ ($\tau_{\lambda^{(n)}}$) are defined as follows

$$I_{\lambda^{(n)}} \equiv I\left(\lambda - \Delta\lambda^{(n)}\right), \quad (12)$$

$$\tau_{\lambda^{(n)}} \equiv \tau\left(\lambda - \Delta\lambda^{(n)}\right). \quad (13)$$

Here $\Delta\lambda^{(n)}$ represents the Doppler shift for the thread $n$ corresponding to its LOS velocity $\xi^{(n)}$ given by

$$\Delta\lambda^{(n)} = \lambda_0 \frac{\xi^{(n)}}{c}, \quad (14)$$

where $\lambda_0$ represents the line-centre wavelength of a given spectral line and $\xi^{(n)}$ is the LOS velocity of thread $n$. Positive values of $\xi^{(n)}$ represent velocities towards the observer.

In Figs. A.1 and A.2, we show the propagation of the H$\alpha$ line through the special configuration of the Model3_6000 at positions 25 and 47 (see Fig. 16) and we follow the value of the Doppler velocity derived from the apparent Doppler shift of the H$\alpha$ profile at each stage. The first plot in the upper left corner represents the outgoing H$\alpha$ profile from the most distant thread in the configuration (thread number 1 in Fig. 16). This H$\alpha$ radiation has to propagate through the next thread on its way towards the observer, where it is partially absorbed. We plot the optical thickness profiles of each following thread in the first column using a red dashed line. The values of the optical thickness are given on the right-hand side axis and range from 0 to 1. If the optical thickness profile was not plotted, this means that the thread in question was geometrically shifted so that its central part with most of the cool prominence plasma is not located in the present LOS (in this case the LOS crossing positions 25 and 47, respectively). Thus, no absorption occurs in the given thread. The H$\alpha$ line profile after the partial absorption is plotted in the second column. The third column displays outgoing H$\alpha$ profiles from the threads themselves (the threads are indicated by numbers corresponding to Fig. 16). The fourth column shows the sum of columns two and three. The fourth-column H$\alpha$ profiles are also displayed in the first-column panels of the next row. The H$\alpha$ profiles and optical thickness profiles of each thread are Doppler-shifted by their respective LOS velocities. The perpendicular dash-dotted line indicates the zero-shift H$\alpha$ line-centre wavelength. The LOS velocities of each thread are indicated in Figs. A.1 and A.2 by "$v$ =" in km s$^{-1}$ (see also Fig. 16). We compute the Doppler shift and resulting Doppler velocity of all H$\alpha$ profiles in the fourth column, and indicate its values by "DopplV =" in km s$^{-1}$.

From these two examples, one can see that the same configuration of the multi-thread model with fixed LOS velocities of each thread can produce, at different positions, synthetic H$\alpha$ line profiles with Doppler shifts corresponding to significantly different velocities. The synthetic H$\alpha$ profile at a given position is the result of integration through several contributing threads with, in general, different LOS velocities. For example, at the position 25 only threads 1, 7, and 9 contribute (see the third column of Fig. A.1), while at the position 47 threads 2, 4, 5, 6, 8, and 10 contribute (Fig. A.2). This shows that although the Doppler velocity of the resulting H$\alpha$ profile mostly corresponds to the motion of the bulk of the prominence mass situated along the given LOS, its value can be significantly lower than the actual LOS velocities of the individual fine structures (as suggested e.g. by Schmieder et al. 2010). Similarly, in cases where many fine structures with generally opposite LOS velocities contribute to the resulting H$\alpha$ intensity obtained along a given LOS, the resulting value of the Doppler velocity can be near zero. On the other hand, in locations such as the edge of a prominence where we can expect only a few, or even a single, fine-structure contribution, the resulting Doppler velocities will be closer to the true velocities of the individual fine structures. This corresponds to the observational findings, such as those of Schmieder et al. (2010), which show that the largest measured Doppler velocities derived from H$\alpha$ prominence observations tend to occur at the prominence edges. This is also true in the case of the studied April 26, 2007 prominence (see Doppler velocity map in Fig. 17), where the highest measured Doppler velocities occur at the edges of the top part of the prominence. The analyses of the Doppler velocities would be further complicated, in the case of a massive prominence, by the presence of regions with optical thicknesses significantly higher than 1 (several units). In such a case, the plasma located further away from the observer will not contribute to the observed H$\alpha$ profile and thus the derived Doppler velocity may not correspond to the real motion of the bulk of the prominence fine structures. However, for the low-mass prominences similar to the one observed on April 26, 2007, the derived Doppler velocities correspond to the motion of the bulk of fine structures, although its values can be reduced by the described integration effect. This can be seen in the bottom part of the Fig. 16, which shows the derived Doppler velocities for each position at the special multi-thread configuration of the Model3_6000. Here, the fine structures with a positive sign of their LOS velocities are mostly shifted to the left, while those with negative LOS velocity signs are displaced to the right. This agrees with the Doppler velocities displayed in Fig. 16.

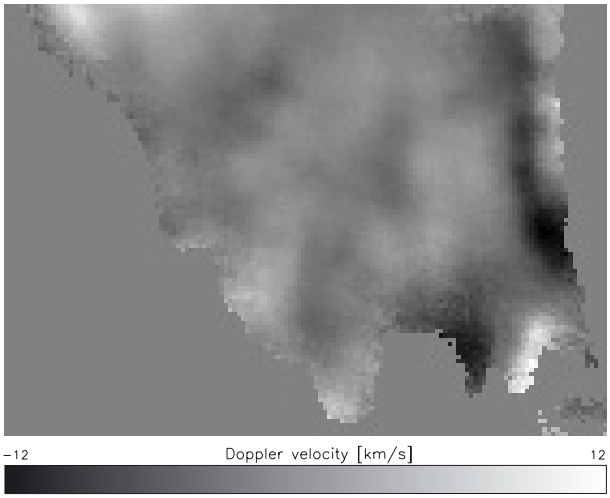


**Fig. 17.** Doppler velocity map of the April 26, 2007 prominence. Upper boundary of the figure is parallel to the solar limb.

### 5.2. Doppler velocities – statistical analysis

A local pixel-to-pixel analysis of the Doppler velocities derived from the H$\alpha$ line profiles might lead to a somewhat uncertain characterization of the real velocity fields of the observed prominences. This can be supported by an analysis of the whole data-set of the observed prominence and by comparison with the synthetic H$\alpha$ spectra produced by realistic prominence fine-structure models. This statistical approach implicitly takes into

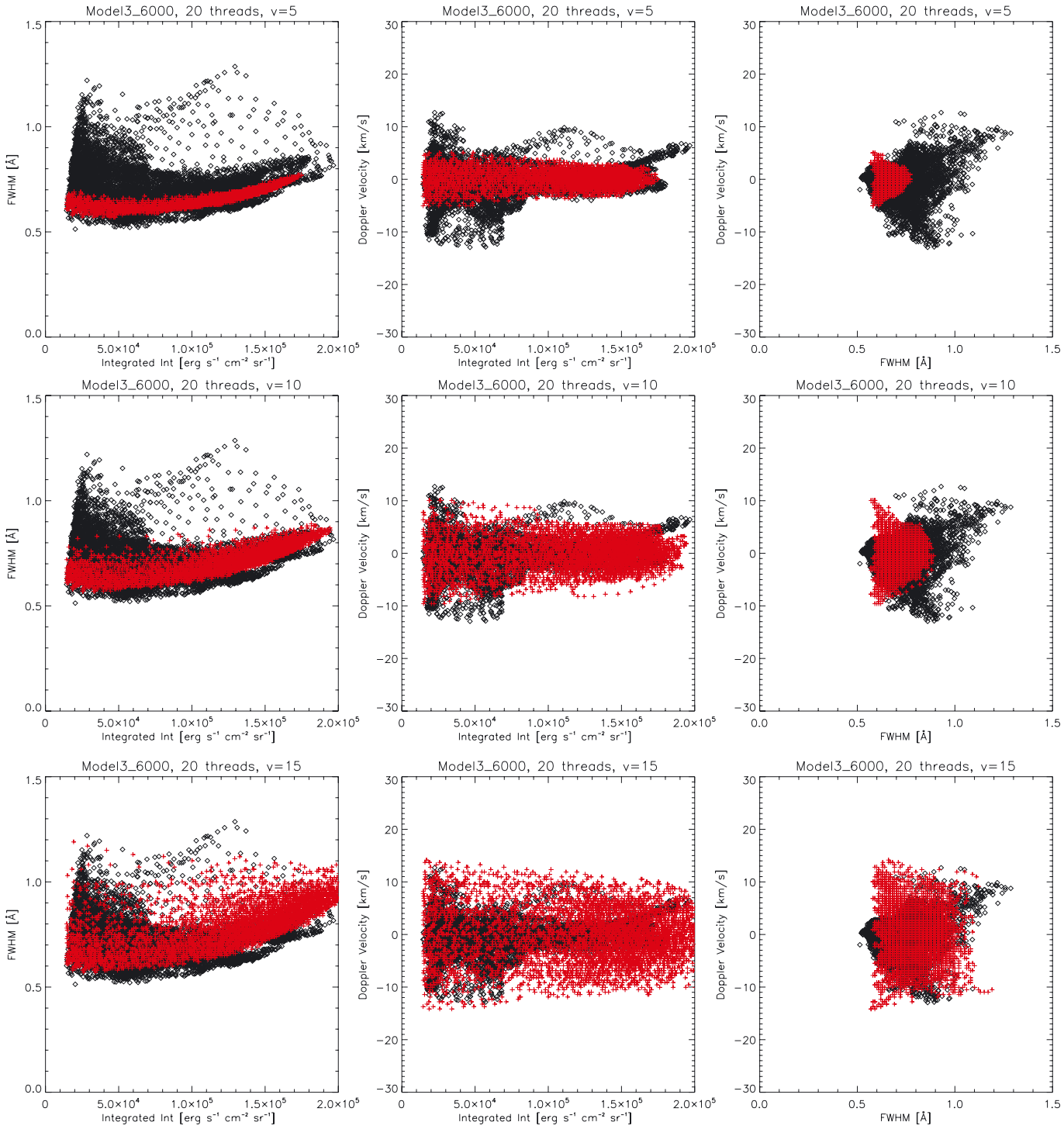


**Fig. 18.** Scatter plots of the line integrated intensity as a function of FWHM (*first column*), integrated intensity as a function of the Doppler velocity (*second column*), and FWHM as a function of the Doppler velocity (*third column*). The observed data are represented by black diamonds and the synthetic data from 100 random realizations of the Model3_6000 with 20 threads and LOS velocities from intervals ⟨–5, 5⟩ (*first row*), ⟨–10, 10⟩ (*second row*), and ⟨–15, 15⟩ km s$^{-1}$ (*third row*) by red crosses.

account any effect of the line propagation through multiple fine structures, thus can be helpful in investigating the prominence velocity fields.

We again use the Model3_6000 with 20 threads and LOS velocities from intervals ⟨–5, 5⟩, ⟨–10, 10⟩, and ⟨–15, 15⟩ km s$^{-1}$. Figure 18 shows scatter plots of the line integrated intensity as a function of the line FWHM (first column), integrated intensity as a function of the Doppler velocity (second column), and the line FWHM as a function of the Doppler velocity (third column). The observed data are represented by black diamonds and the synthetic data of one hundred random realizations of the given model by red crosses. Here, one can see that while the model with the LOS velocity interval of ⟨–5, 5⟩ (first row) agrees with the most of the Doppler velocities of the more intense part of the observed prominence, it is the model for the LOS velocity interval of ⟨–10, 10⟩ (second row) that also has good agreement with the Doppler velocities of the lower intensity part of the prominence. It also agrees with the majority of the FWHM

versus integrated intensity distribution. On the other hand, the model with the LOS velocities from the interval of ⟨–15, 15⟩ (third row) produces too wide a spread in the Doppler velocities with respect to the observed integrated intensities. Thus, one can argue that the overall distribution of the LOS velocities in the April 26, 2007 prominence at the time of the observations was below ±15 km s$^{-1}$ and for the higher intensity part close to ±10 km s$^{-1}$. The observed data show that the lower-intensity H$\alpha$ profiles (situated preferentially at the prominence edges) may have higher Doppler velocities than the higher intensity ones. This agrees with our previous arguments and also with the observed data (see Fig. 17).

## 6. Discussion and conclusions

We have employed the 2D multi-thread prominence fine-structure models to obtain the synthetic Lyman lines and H$\alpha$ line that we use to analyze the dynamics of the quiescent prominence observed on April 26, 2007. This well-observed prominence that occurred for three consecutive days was previously analyzed by several authors. Berlicki et al. (2011) and Labrosse et al. (2011) analyzed the observations obtained on April 26, 2007, while Heinzel et al. (2008), Berger et al. (2010), and Schmieder et al. (2010) focused on a prominence that occurred on April 25, 2007. Our present investigation extends that of Berlicki et al. (2011) by focusing on the statistical analysis of the H$\alpha$ line with emphasis on the dynamics of the prominence fine structures.

To begin the investigation, we derived a multi-thread model with randomly distributed LOS velocities of randomly shifted threads (see Fig. 8) that produces synthetic Lyman spectra in good agreement with the spectra observed by SOHO/SUMER. We started with the Model2 of Berlicki et al. (2011), then derived, by trial-and-error, Model3, and then the variations of these models (for model parameters, see Table 1). For a statistical comparison of the synthetic and observed H$\alpha$ line profiles, we chose three parameters, namely the integrated intensity, the FWHM, and the Doppler velocity derived from shifts of the line profiles. This combination of statistical parameters allowed us to analyze not only the impact of the model input parameters on the synthetic H$\alpha$ intensities but also the effect of the LOS velocities on the shape of the line profiles. Even more interestingly, this statistical approach could help us to determine the prominence core temperatures. In our models, this is given by parameter $T_0$ – the minimum central temperature. The value of this parameter has an effect on the thermal broadening of the H$\alpha$ line profiles, thus a lower value of $T_0$ should statistically lead to narrower profiles. This is indeed true, as can be seen by either comparing Model2 (Fig. 10 – right) with Model2_5000 (Fig. 12), or Model3 (Fig. 14 – right) with Model3_6000 (Fig. 15). In both cases, the latter model with the lower value of $T_0$ (5000 K, respectively, 6000 K compared to 8000 K, see Table 1) produces synthetic H$\alpha$ profiles with the minimum FWHM values in better agreement with the observed data than the hotter models. At the same time, the lower $T_0$ values do not affect either the shape or intensity of the Lyman line profiles significantly, which leads us to conclude that the cooler models provide a closer description of the observed prominence. We note that the value of the central minimum temperature does not strongly affect the synthetic spectra produced by only relatively low-mass low-pressure models, such as either Model2 or Model3 (as argued by Gunár et al. 2011b). In contrast, the value of $T_0$ has a strong influence on the synthetic Lyman line profiles of more massive models producing reversed profiles when observed across the magnetic field lines.

The spread in the line FWHM can also serve as a good indicator of the statistical distribution of the LOS velocities in the observed prominence. The larger LOS velocities we assume in the model, the wider the spread of the synthetic FWHM (see e.g. Fig. 11). This, together with the direct analysis of the Doppler velocities, leads us to conclude that the overall statistical distribution of the LOS velocities in the April 26, 2007 prominence at the time of observations was narrower than ±15 km s$^{-1}$. This agrees with the findings of Schmieder et al. (2010), who analyzed the dynamics of the April 25, 2007 prominence and reported the average LOS velocities to be on the order of ±5 km s$^{-1}$ with some parts lying mostly at the prominence edges showing velocities up to ±15 km s$^{-1}$.

Because we used a simplified multi-thread model with identical threads we were unable to explain the whole observed H$\alpha$ data-set. Although the models presented here were in good agreement with the bulk of the mostly higher-intensity profiles, part of the observed data consists of mostly low-intensity profiles with larger FWHM values and also larger Doppler velocities. Thus, as can be deduced from Fig. 18, the true range of the LOS-velocity distribution of the main higher-intensity part of the April 26, 2007 prominence could be close to ±10 km s$^{-1}$. The lower-intensity H$\alpha$ profiles with larger FWHM and Doppler velocities could be situated at prominence edges where the lower electron-density values would lead to less intense profiles despite the higher ionization of the prominence plasma. At the same time, the observed prominence edges have higher Doppler velocities (see Fig. 17) corresponding to larger FWHM values. Thus, the weaker observed H$\alpha$ profiles might have preferentially larger widths than the stronger ones, which can explain the excess of observed data with relatively large FWHM at low intensities (see the observed data scatter plot of integrated intensities versus FWHM). These scatter plots also show interesting curved trends at the lowest FWHM values with respect to increasing intensity. However, this trend is probably not linked to the LOS velocities but can instead be explained by saturation effects at higher intensities. This means that the more intense H$\alpha$ profiles cannot have FWHM as low as the profiles with much lower intensities.

Present investigation shows that the prominence observed on April 26, 2007 had rather low-mass and weakly magnetized structure with the horizontal magnetic-field strength of around 5 gauss (see Table 1). This corresponds to the findings of previous studies (Berger et al. 2010; Berlicki et al. 2011; Heinzel et al. 2008; Labrosse et al. 2011; Schmieder et al. 2010; Török et al. 2009) of this prominence passing over the limb between April 24 and April 26, 2007. Several of these authors used standard assumptions for the minimum prominence-core temperature of 8000 K (Heinzel et al. 2008, assumed temperatures from 6000 to 8000 K). As our detailed statistical analyses showed, this assumption is relevant to the observed prominence. However, models with lower values (5000 and 6000 K, respectively) provide better agreement between observed and synthetic FWHM values.

To perform a statistical analysis similar to that presented here, one needs to observe prominences in the H$\alpha$ spectral line with high spatial and high spectral resolutions, of course preferably in coordination with other spaceborne or ground-based instruments. This highlights the importance of instruments that have simultaneous imaging and spectroscopic capabilities, such as the Meudon/MSDP spectrograph or for example the Bialkow/MSDP spectrograph (Rompolt et al. 1994), 2D imaging spectro-polarimeter ZIMPOL II (Zurich Imaging Polarimeter, Gandorfer et al. 2004), and IBIS (Interferometric BIdimensional

Spectrometer, Cavallini 2006) at Dunn Solar Telescope of the National Solar Observatory. A new-generation MSDP spectrograph is also planned for the EST (European Solar Telescope).

*Acknowledgements.* S.G. acknowledges the support from grants 250/09/P554 and 209/12/0906 of the Grant Agency of the Czech Republic. P.H. acknowledges the support from grant 209/12/0906 of the Grant Agency of the Czech Republic. S.G. and P.H. acknowledge the support from the Observatoire de Paris, Section de Meudon. Space-based observations were obtained during a MEDOC coordinated campaign managed by N. Labrosse. Authors also acknowledge G. Molodij for the Meudon/MSDP observations. The authors acknowledge support from the International Space Science Institute, Bern, Switzerland to the International Team 174. Work of S.G. and P.H. was supported by the project RVO: 67985815.

## References

Anzer, U., & Heinzel, P. 1999, A&A, 349, 974
Berger, T. E., Slater, G., Hurlburt, N., et al. 2010, ApJ, 716, 1288
Berlicki, A., Gunar, S., Heinzel, P., Schmieder, B., & Schwartz, P. 2011, A&A, 530, A143
Cavallini, F. 2006, Sol. Phys., 236, 415
Curdt, W., Brekke, P., Feldman, U., et al. 2001, A&A, 375, 591
David, K.-H. 1961, ZAp, 53, 37
Gandorfer, A. M., Steiner, H. P. P. P., Aebersold, F., et al. 2004, A&A, 422, 703
Gunár, S., Heinzel, P., Schmieder, B., Schwartz, P., & Anzer, U. 2007, A&A, 472, 929
Gunár, S., Heinzel, P., Anzer, U., & Schmieder, B. 2008, A&A, 490, 307
Gunár, S., Schwartz, P., Schmieder, B., Heinzel, P., & Anzer, U. 2010, A&A, 514, A43
Gunár, S., Heinzel, P., & Anzer, U. 2011a, A&A, 528, A47
Gunár, S., Parenti, S., Anzer, U., Heinzel, P., & Vial, J.-C. 2011b, A&A, 535, A122
Harrison, R. A., Sawyer, E. C., Carter, M. K., et al. 1995, Sol. Phys., 162, 233
Heinzel, P., & Anzer, U. 2001, A&A, 375, 1082
Heinzel, P., Anzer, U., & Gunár, S. 2005, A&A, 442, 331
Heinzel, P., Schmieder, B., Fárník, F., et al. 2008, ApJ, 686, 1383
Kippenhahn, R., & Schlüter, A. 1957, Z. Astrophys., 43, 36
Kotrč, P. 2009, Central Eur. Astrophys. Bull., 33, 327
Labrosse, N., Heinzel, P., Vial, J., et al. 2010, Space Sci. Rev., 151, 243
Labrosse, N., Schmieder, B., Heinzel, P., & Watanabe, T. 2011, A&A, 531, A69
Lin, Y., Engvold, O., Rouppe van der Voort, L., Wiik, J. E., & Berger, T. E. 2005, Sol. Phys., 226, 239
Mein, P. 1991, A&A, 248, 669
Rompolt, B., Mein, P., Mein, N., Rudawy, P., & Berlicki, A. 1994, in JOSO Annual Report 1993, ed. A. V. Alvensleben, 87
Schmieder, B., Gunár, S., Heinzel, P., & Anzer, U. 2007, Sol. Phys., 241, 53
Schmieder, B., Chandra, R., Berlicki, A., & Mein, P. 2010, A&A, 514, A68
Schühle, U. 2003, SUMER Data Cookbook, Published on internet at http://www.mps.mpg.de/projects/soho/sumer/text/cookbook.html
Török, T., Aulanier, G., Schmieder, B., Reeves, K. K., & Golub, L. 2009, ApJ, 704, 485
Tsuneta, S., Ichimoto, K., Katsukawa, Y., et al. 2008, Sol. Phys., 249, 167
Wilhelm, K., Curdt, W., Marsch, E., et al. 1995, Sol. Phys., 162, 189

Pages 14 to 15 are available in the electronic edition of the journal at http://www.aanda.org

## Appendix A:

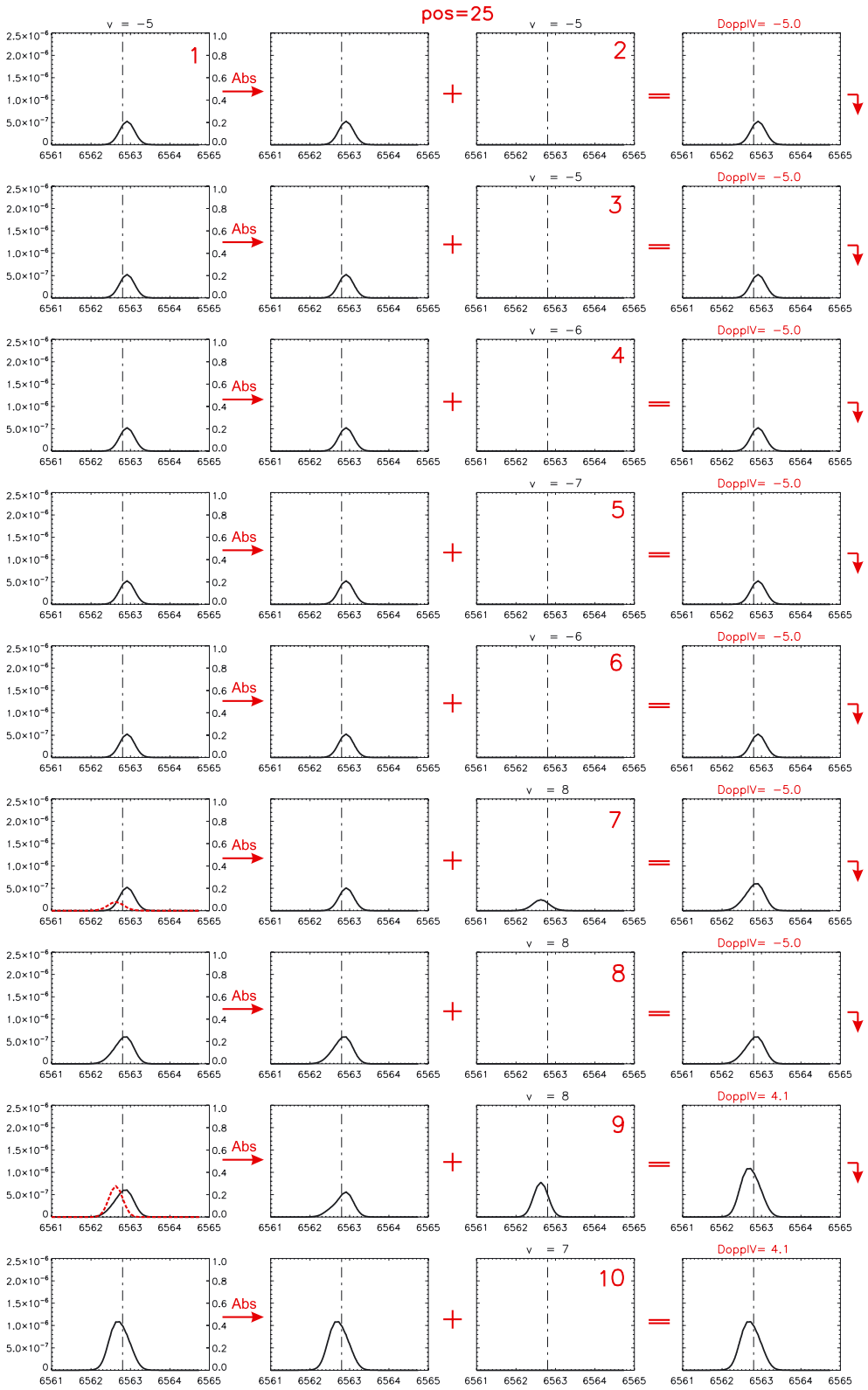


**Fig. A.1.** Details of the formation of the H$\alpha$ line within a special multi-thread configuration of the MODEL3_6000 (see Fig. 16, top) at the position 25. The *first plot* at the *upper left corner* represents the outgoing H$\alpha$ profile from the last thread in the configuration. In the rest of the *first column*, we plot the same H$\alpha$ profiles as in the *fourth column* in the row above and also the optical thickness profiles (red dashed line) of the threads where the respective absorption occurs. Values of the optical thickness are given on the right-hand side with ranges of from 0 to 1. The *second column* shows H$\alpha$ profiles after the respective partial absorption. The *third column* displays outgoing H$\alpha$ profiles from the threads themselves (threads are indicated by numbers) and the *fourth column* shows the sum of columns two and three. The perpendicular dash-dotted line indicates the zero-velocity H$\alpha$ line centre wavelength. The LOS velocities of each thread are indicated by "$v$ =" in km s$^{-1}$. The derived Doppler velocities of all H$\alpha$ profiles in the *fourth column* are indicated by "DopplV =" in km s$^{-1}$.

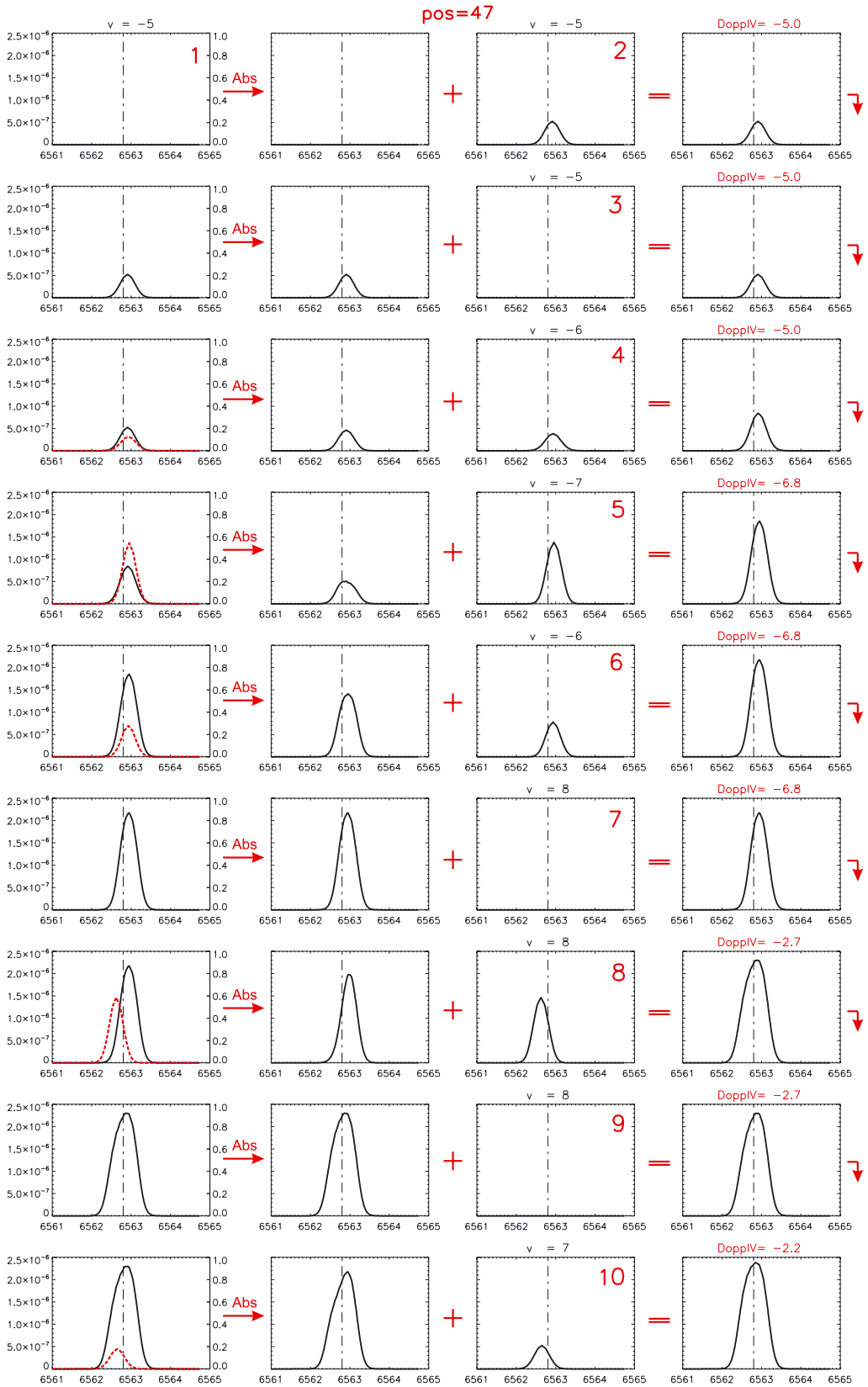


**Fig. A.2.** The same as in Fig. A.1 but at the position 47.